The International Journal of Advanced Manufacturing Technology (2024) 130:1321–1339
https://doi.org/10.1007/s00170-023-12785-0

ORIGINAL ARTICLE

Microstructure and selected properties of the solution heat-treated MAR-M247 Ni-based superalloy fabricated via directional solidification

Łukasz Rakoczy[1] · Małgorzata Grudzień-Rakoczy[2] · Rafał Cygan[3] · Tomasz Kargul[1] · Anna Zielińska-Lipiec[1]

Received: 20 September 2023 / Accepted: 1 December 2023 / Published online: 9 December 2023

Abstract

This work focuses on MAR-M247 Ni-based superalloy manufactured via directional solidification at various withdrawal rates (3.4 or 5.0 mm/min) and shell mold temperatures (1510 °C or 1566 °C) after solution heat-treatment (SHT). Observations and analyses of four casting variants were carried out using thermodynamic simulations, differential scanning calorimetry (DSC), X-ray diffraction (XRD), light microscopy (LM), scanning electron microscopy (SEM), X-ray spectroscopy (EDX), and tensile tests at ambient temperature. The solidus and liquidus temperatures were very similar for all variants and were in the range of 1263–1264 °C and 1356–1359 °C, respectively. The presence of the γ, γ', MC carbides, and M_5B_3 phases was confirmed. Microstructure differences were observed depending on the manufacturing parameters. The castings' dendritic regions consisted of γ' precipitates surrounded by the matrix, with a mean size ranging from 0.203 to 0.250 µm, depending on the casting parameters. The amount of the MC carbides in the interdendritic spaces was in the range of 1.87–1.92%. The tensile tests determined that castings produced with preheat temperature of 1566 °C were characterized by higher elongation and slightly lower yield strength in comparison to 1510 °C.

Keywords Directional solidification · Superalloy · Aerospace · Casting · Solution

1 Introduction

Directionally solidified Ni-based superalloys are widely used in jet engines, especially in large-scale and geometrically complex blades. In contrast to the equiaxed grains, the columnar grain structures remove grain boundaries transverse to the main tensile stress axis, enhancing creep resistance by limiting cavitation and cracking along them [1, 2]. The excellent strength of cast Ni-based superalloys at service conditions originates mainly from γ' precipitates possessing an ordered $L1_2$ structure, which is coherent with the disordered γ matrix [3]. However, coarse and irregularly shaped secondary γ' precipitates, significant volume fractions of the γ-γ' eutectic phase and strong dendritic segregation within the superalloys inhibit their use directly in the as-cast state. Therefore, efforts need to be made to obtain the appropriate morphology and stereological parameters of the γ' precipitates [4]. High creep resistance can be reached when the matrix is reinforced with cubic particles in the range of 0.35–0.50 µm [5]. The morphology and size of the γ' precipitates can be controlled by selecting the appropriate temperature and heat treatment duration [6–8], whereas the volume fraction depends mainly on the Al concentration. Solution heat-treatment (SHT) is widely applied before aging in Ni-based superalloys and constitutes an important stage in the shaping the final components' high-temperature strength. The process should lead to the completely dissolution of secondary γ' and some minor phases, partially dissolving primary γ', as well as reducing the dendritic segregation of alloying elements during solidification [9, 10]. During subsequent cooling, γ' phase nuclei precipitate out again, and growth. The volume fraction of the γ' precipitates can then be adjusted via aging [11, 12]. Theoretically, the SHT temperature for Ni-based superalloys should be between the γ' solvus and bulk solidus temperatures. From the industrial point of view, increasing the temperature and shortening the holding

✉ Łukasz Rakoczy
lrakoczy@agh.edu.pl

[1] Faculty of Metals Engineering and Industrial Computer Science, AGH University of Kraków, Mickiewicza 30, 30-059 Kraków, Poland

[2] Łukasiewicz Research Network-Kraków Institute of Technology, Zakopiańska 73, 30-418 Kraków, Poland

[3] Consolidated Precision Products Corporation, Investment Casting Division, Hetmańska 120, 35-078, Rzeszow, Poland

time would be most optimal; however, this approach cannot be used in this case. The superalloy's chemical composition includes many alloying elements, so their segregation during non-equilibrium solidification limits this temperature range due to increased susceptibility to incipient melting below the bulk solidus temperature [13, 14]. In industrial practice, this window can be limited to 50–150 °C. Although secondary γ' precipitates dissolve quickly, a substantial amount of time is necessary for the partial dissolution of primary γ', dissolution of minor phases and limiting dendritic segregation due to several heavy elements that diffuse slowly in the γ phase [15]. The MAR-M247 alloy developed by the Martin-Marieta Company is one of the most widely used Ni-based superalloy both in equiaxed and directionally-solidified variants in aircraft engines, with many studies dedicated to property optimization. Baldan [16] observed during solution treating (1250 °C/310 min) of equiaxed MAR-M247 rotor castings that the chemical composition of MC carbides becomes enriched in Hf and depleted in Ta. Furthermore, it was found that residual Al segregation after treating led to localized formation of large γ' precipitates after subsequent one-step aging at 770 °C or 870 °C. Silva [17] investigated the possibility of replacing expensive Ta by Nb. Observations after SHT at 1260 °C showed the reduction in alloying element segregation and partial carbide dissolution as a function of holding time. After 2 h, the dendritic and interdendritic regions were clearly visible, while after 4 h, these regions were partially homogenized; however, a chemical concentration gradient was still present. After 8 h, a highly homogeneous γ matrix was obtained, with those parameters determined as the optimum SHT. Increasing the SHT temperature to 1280 °C caused γ-γ' incipient melting, which is not surprising as the temperature is close to bulk solidus. Industrial practice maintains the servicing of MAR-M247 components under fully heat-treated conditions [18]. Costa [19] fabricated as-cast DS MAR-M247 (withdrawal rate 18 cm/h and fixed thermal gradient of 80 °C/cm) with a yield strength (YS) of 796 and 671 MPa at room temperature and 600 °C, respectively (compression tests). Bor [20] investigated the mechanical properties of DS MAR-M247 (withdrawal rate of 180 mm/h) under fully heat-treated conditions. The ultimate tensile strength (UTS) of the produced castings was around 1000 MPa, whereas at 982 °C it dropped to the around 650-750 MPa. In accordance with standard requirements [21], after creep testing at 760 °C/724 MPa, the elongation of MAR-M247 should be greater than 2% (creep life > 23 h), while elongation during tensile testing at 899 °C should exceed 4%. The MAR-M247 superalloy's high brittleness can lead to manufacturing problems like hot cracking and misruns during castings and welding [22]. Technological parameters selected for component fabrication act on the cooling rate, which influences the dendritic microstructure of castings, precipitate size, their distribution, and morphology, as well as alloying element microsegregation. This means that the superalloy's response to SHT, i.e., the degree of precipitates dissolution, chemical composition homogenization, strength, and ductility may exhibit differences. From the point of view of later aging, this may play an important role in optimizing the key functional properties during use.

This work focuses on studying the microstructure and selected properties of the directionally solidified MAR-M247 Ni-based superalloy produced with two different withdrawal rates and two shell mold temperatures. Detailed investigations into these aspects after SHT will facilitate generating the optimal preconditions for further phase transformations occurring during aging, which is important in obtaining a broader understanding on the influence of fabrication parameters on the MAR-M247 superalloy.

2 Materials and methodology

The experimental castings (equipped with a gating system) used in this work were made of the DS MAR-M247 Ni-based superalloy, with a nominal chemical composition presented in Table 1.

The setup comprised of a cooling plate base, construction pin, pouring pan, and eight castings (length 250 mm and diameter 14 mm). Additional vents were prepared to stabilize and reinforce the wax models and facilitate proper autoclave dewaxing. Each wax set was strengthened with ceramic bars for structure stiffening and an in-house designed grip allowed to mount the sets in a robotic station for cleaning and shell mold preparation. Each layer was created via the dip and stucco technique, i.e., by dipping the wax set patterns into a binder and filler (slurry) and subsequent covering by the coarse dry backup. The dried molds were dewaxed, burned out, and covered by heat insulation (Fiberfrax). The directional solidification process was performed in a vertical Bridgman vacuum furnace ALD VIM-IC 2 E/DS/SC (ALD Vacuum Technologies GmbH). Each ceramic mold was mounted in the furnace chamber preheated to T_0 temperature (1510 °C or 1566 °C) (Table 2). The 4.5-kg MAR-M247 ingot was inductively melted in a vacuum of 2.9×10^{-3} Pa. After heating up the furnace to 1600 °C and holding

Table 1 Nominal chemical composition of DS MAR-M247 Ni-based superalloy, wt %

Element	Co	W	Cr	Al	Ta	Hf	Ti	Mo	Zr	B	C	Ni
Concentration	10.0	10.0	8.40	5.50	3.0	1.4	1.1	0.65	0.05	0.015	0.15	Bal.

Table 2 Directional solidification casting parameters

Casting	Shell mold temperature, °C	Pouring temperature, °C	Withdrawal rate, mm/min
LP3W	1510	1538	3.4
LP5W			5.0
HP3W	1566		3.4
HP5W			5.0

for 0.5 h, withdrawal was initiated at an established rate. The pouring temperature was 1538 °C, so in variants LP3W and LP5W, T_0 was lower than that, while in variants HP3W and HP5W, T_0 was higher. During directional solidification and cooling of the ingots, a preferred orientation of grains was developed. When solidification ended, the molds were cooled to ambient temperature, the casts were knocked out, and experimental rods were mechanically cut out.

Thermodynamic simulations, using the ThermoCalc software (database TCNI10:Ni-Alloys), were carried out to predict the phase stability in the temperature range from 700 to 1400 °C. To analyze the phase transformation temperatures and thermal effects occurring during the heating of the superalloy castings, differential scanning calorimetry (DSC) was performed with Netzsch STA 449F3 Jupiter equipped with a rhodium furnace operating up to 1600 °C. The calibration procedure included notating temperatures and melting enthalpies of standard elements (Ni, Au, Al, Sn, In) and comparing the obtained values with nominal values. Vacuum in the furnace chamber was made twice and then filled with Ar (purity of 6N). The additional zirconium oxygen trap was applied to tie up the residual oxygen and protect the samples from oxidizing. The experiments involved heating the samples (in Al_2O_3 85 µl crucibles with lids) from 25 to 1460 °C (10 K/min). The sample mass did not change during heating, therefore the oxidation process of the MAR-M247 and chemical composition variations were negligible. The registered sample values were corrected for the values from device calibration, enabling the quantitative analysis of the thermal melting effects.

X-ray diffraction was performed in the range of 2θ = 30–120° to identify the castings' phase composition. Measurements were performed on mechanically polished specimens (with a diameter of 14 mm and height of 5 mm) in Bragg-Brentano geometry using a Bruker D8 Advance diffractometer (λ_{Co} = 1.789 Å). Microstructure analysis was carried out on samples cut off from each of the four castings. The preparation procedure included grounding on sandpaper, polishing on diamond suspension and colloidal silica, and a final chemical etching process in a reagent: 25 ml water, 25 ml HCL, 25 ml HNO_3, 1.5 g H_2MoO_4. Observations were carried out with a Leica DM1000 light microscope (LM) and scanning electron microscope (SEM) Phenom XL (ThermoFisher) with a 20 kV accelerating voltage. Quantitative analysis of the captured back-scattered electron (BSE) images was carried out via ImageJ. According to the Cavalieri-Hacquert principle, the relative volume occupied by a selected constituent is the area fraction taken by it on the unit surface of the sample. The volume fraction of secondary γ' precipitates (mag. ×25k) in dendritic regions and MC carbides (mag. ×1k) was evaluated by the planimetric method (Eqs. 1 and 2).

$$V_v = A_A \tag{1}$$

$$A_A = \left(\frac{\Sigma A_i}{A}\right) \times 100\% \tag{2}$$

where V_v is the total volume of the phase object per unit volume of the superalloy, µm^3/µm^3; A_A is the total field flat sections on the individual phase of the image per unit area, µm^2/µm^2; A_i is the total field of flat sections on the individual i-phase, µm^2; and A is the total image area, µm^2.

Considering that γ' precipitates in the superalloy usually take on a cubic-like shape, their mean size in this work was expressed as the square's side of precipitates (square root of precipitates' area) (Eq. 3). Measurements were carried out in 25 locations within the dendritic regions using captured images (magnification ×25k). Binarization and de-spackle filtering was used to remove noise without blurring edges on SEM-BSE microstructure images. Only γ' precipitates characterized by an area in the range of 0.02–1.0 µm^2 were analyzed.

$$\overline{D} = \overline{d} = \sqrt{\mathrm{A}} \tag{3}$$

where A is the area of γ' precipitate.

Chemical composition analysis of selected regions was carried out via X-ray dispersive spectroscopy (SEM-EDX). Firstly, to reveal relative composition differences between the dendritic regions and interdendritic spaces, the partition coefficient was calculated. To this end, 40 measurements were performed for each casting variant in accordance with Eq. 4.

$$k^{\mathrm{i}} = \frac{C_{\mathrm{D}}^{\mathrm{i}}}{C_0^{\mathrm{i}}} \tag{4}$$

where $C_{\mathrm{D}}^{\mathrm{i}}$ is the "*i*" element concentration in the dendrite core (point analysis), and C_0^{i} is the "*i*" element concentration in the area 53 × 53 µm (area including dendritic cores and interdendritic spaces).

Additionally, chemical composition analysis of MC carbides and primary γ' was performed to determine the relationship between selected alloying elements. Point and area measurements were gathered for 90 s (more than one million

counts), whereas for maps the duration was set to approx. 1 h (ZAF correction). The tensile tests performed at ambient temperature were carried out on round threaded specimens prepared following the ASTM E8/E8M (diameter 6 mm, gage length 30 mm) requirements using a Zwick 250 kN machine. Measurements were performed with an initial force of 2200 N at a constant rate of 0.004.

3 Results and discussion

3.1 Phase stability analysis via ThermoCalc and DSC

Under equilibrium conditions, γ' was the main strengthening phase, dominating the structure up to 1040 °C (Fig. 1a). With further temperature increase, the γ matrix predominates. The solvus temperature of the γ' phase is 1220 °C. The data indicate that $M_{23}C_6$ carbides are more stable than MC in the medium temperature range, suggesting the possibility of an MC + $\gamma \rightarrow \gamma' + M_{23}C_6$ phase transformation during annealing. At high temperatures (exceeding 1009 °C) MC carbides dominate over $M_{23}C_6$. The solvus temperature of $M_{23}C_6$ carbides is 1039 °C. Precipitates of M_5B_3 borides are very stable up to 1009 °C. After exceeding this temperature, they rapidly dissolve, with the possibility of local liquid phase appearance due to matrix enrichment in B. The liquidus temperature is 1390 °C.

DSC curves registered during specimen heating are presented in Fig. 1b. The first extensive exothermic effect is revealed, occurring in the range of 1200–1290 °C, associated with the dissolution of γ' phase precipitates. Subsequently, the endothermic effect related to sample melting is present. The γ-γ' eutectic precipitates could possibly be the first phase to melt. The maximum temperature of the peak was taken as the liquidus temperature (T_L) in the tests, while the solidus temperature (T_S) was defined as the start of the disturbance associated with melting. The melting enthalpy is very similar and equal to the 140–164 J/g (Table 3).

3.2 Casting structure characterization

Based on the XRD spectra, the γ matrix, intermetallic γ' phase, MC carbides, and M_5B_3 borides were all identified (Fig. 2). The orientation of the matrix is <001> induced by directional solidification. Minor phases like $Ni_7(Hf, Zr)_2$ and M_3C_2 carbides present in as-cast condition were dissolved during SHT [23]. Chemical etching of the sample revealed a typical dendritic structure (Fig. 3). Features of the superalloy's primary structure were still visible after heat treatment. The dendritic areas (primary dendrite cores and secondary arms of dendrites) are characterized by a relatively homogenous microstructure, while numerous γ-γ' eutectic islands and carbide-looking precipitates can be seen in the interdendritic spaces. The SHT dissolved the minor phases mentioned above and simultaneously did not led to local incipient melting.

To present the differences in selected alloying element distribution in the castings' microstructure, a semi-quantitative SEM-EDX analysis was carried out. Using the obtained

Table 3 Liquidus temperature (T_L), solidus temperature (T_S), and melting enthalpy (ΔH_m) of castings

Casting	Incipient melting T_S, °C	Liquidus T_L, °C	Enthalpy of melting ΔH_m, J/g
LP3W	1293	1359	140
LP5W	1294	1357	141
HP3W	1293	1357	160
HP5W	1293	1356	145

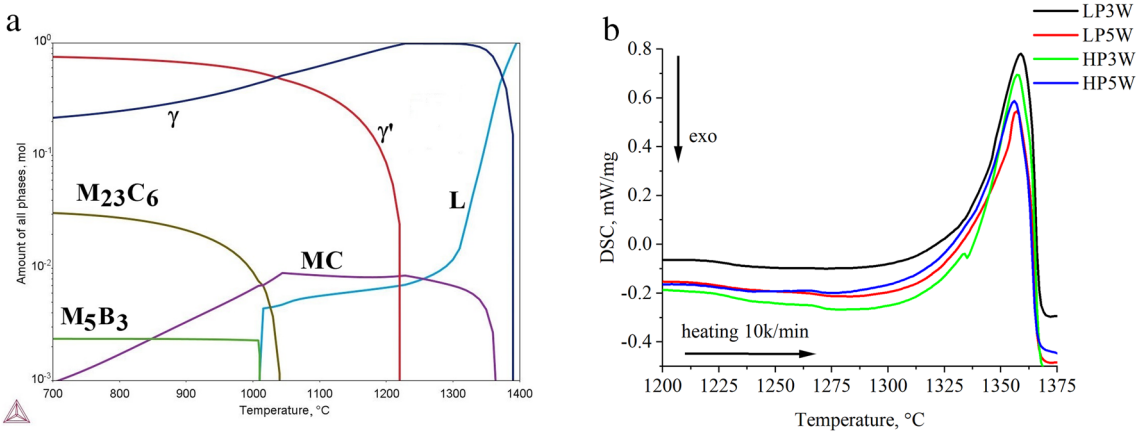

Fig. 1 **a** Phase stability with increasing temperature under equilibrium conditions. **b** DSC curves of the DS MAR-M247 castings registered during heating

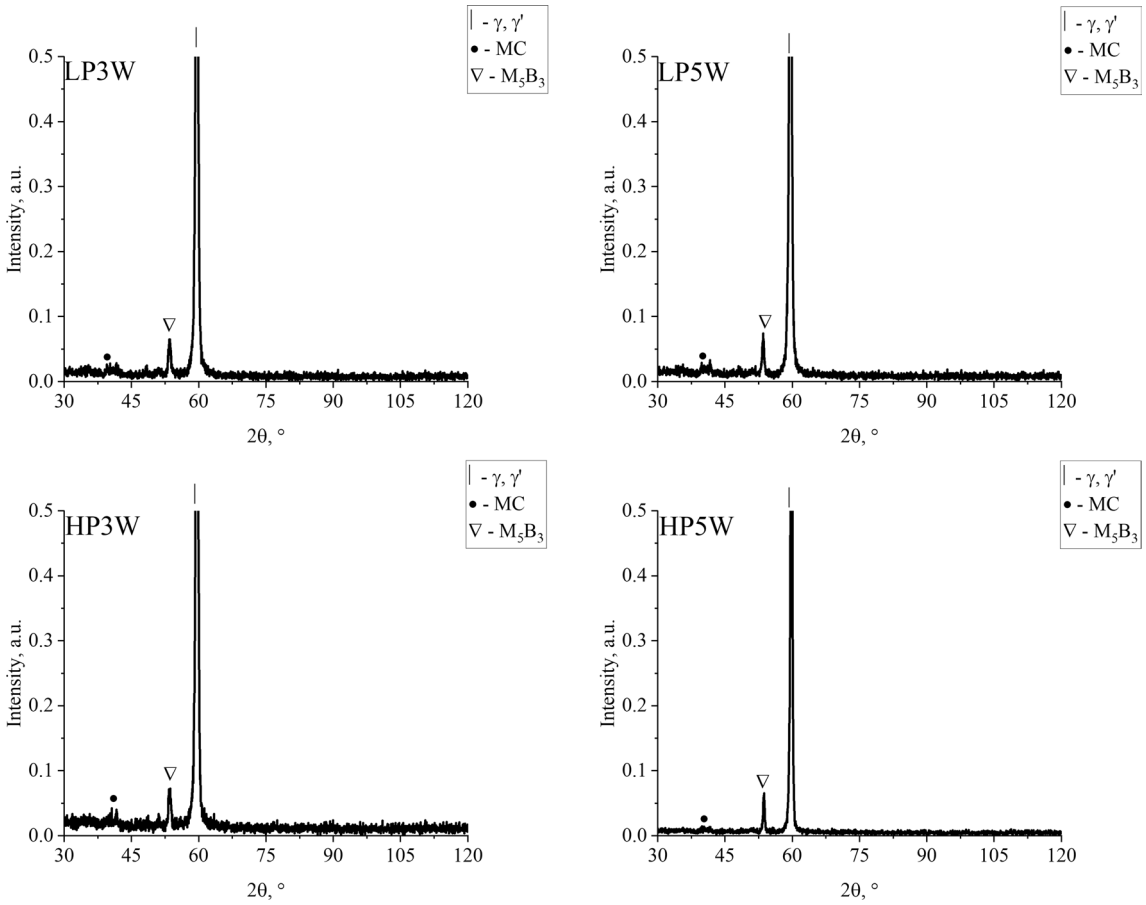

Fig. 2 X-ray diffraction pattern of the DS MAR-M247 castings after SHT

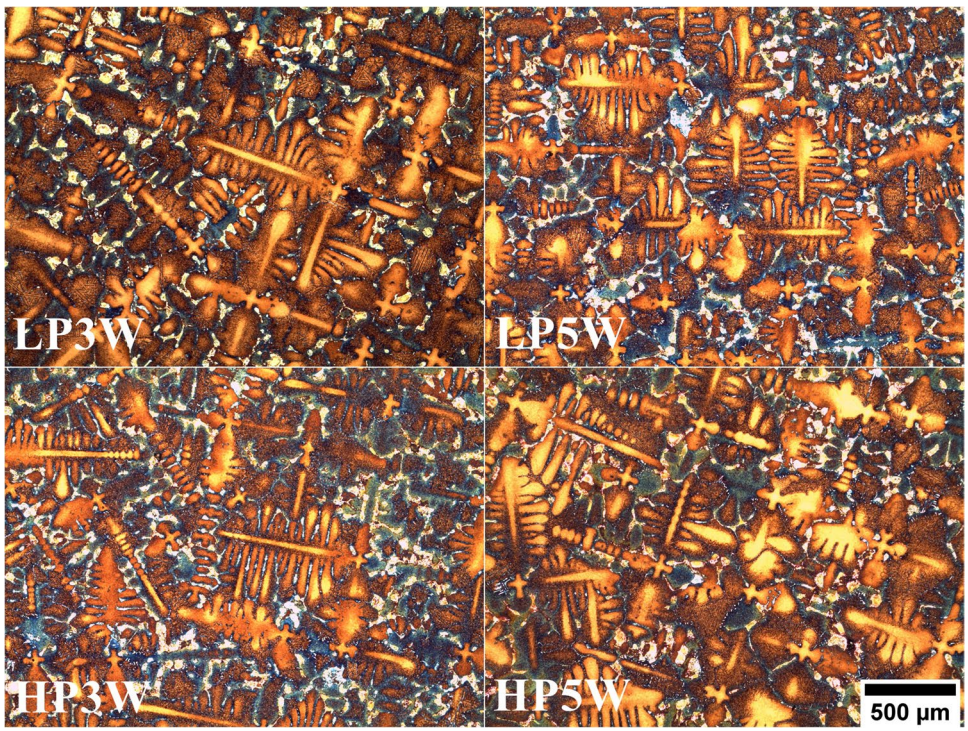

Fig. 3 Dendritic microstructure of the DS MAR-M247 castings after SHT, LM

results, the partitioning coefficient $k^i = \frac{C_D^i}{C_0^i}$ was calculated. The k^i coefficient for the alloying elements is presented in Table 4. A $k^i < 1$ value suggests that the element segregates to the interdendritic spaces, which was the case for Hf and Ti (strong carbide-formers). The k^{Ni}, k^{Co}, and k^{Cr} coefficients are close to 1, indicating a relatively homogenous distribution in the castings, as these alloying elements are a mainly part of the γ phase. Higher element concentration in the dendritic regions is indicated by a $k^i > 1$, values obtained for W, Mo, and Al. As the diffusion of W is sluggish, its transport from the liquid phase to γ is not completely obtained using the usual cooling rates. Silva [17], based on the SEM-EDX analysis of the MAR-M247 superalloy after SHT at 1260 °C for 8 h, confirmed a very strong segregation of W in the dendritic areas. A similar $k^W > 1$ was obtained in the Renè 108 Ni-based superalloy after aging treatment [24]. Increased W concentration in the dendritic regions leads to the precipitation of $(Cr, W, Mo)_5B_3$ on the γ/γ' interfaces. Strong enrichment in W would be difficult to reduce even after long-term heat treatment, due to the low solubility of B in γ and γ', so tendency to form borides.

3.3 γ' precipitates morphology analysis

The primary γ' precipitates possessed a diversified distribution and complex morphology (Fig. 4). They formed via the $L \rightarrow \gamma + \gamma'$ phase transformation during directional solidification. Their amount is quite high despite SHT, which indicates a strong residual liquid enrichment in Al during casting solidification. The γ-γ' is an undesirable phase; however, its complete dissolution in MAR-M247 during heat-treatment would risk incipient melting occurring. The presence of Hf in the Ni-based superalloy favors the formation of more γ' primary precipitates [2]. Stereological parameter analysis of γ' precipitates is problematic due to the considerable differences in size and distribution. The chemical composition of the γ' precipitates was analyzed via SEM-EDX (Table 5). They mainly contain Ni and Al, where the ratio between the two is in the range of 3.5–3.7 for all castings. Additionally, the ratio of (Ni, Co)/(Al, Ti, Ta, Hf) was calculated, with Al, Ti, Ta and Hf being γ'-formers, obtaining values of approx. 3.0 and 3.1.

Next, the secondary γ' precipitates found in the dendritic regions were analyzed. The morphology of the secondary γ' precipitates is close to cubic (Fig. 5).

The volume fraction of secondary γ' precipitates in the dendritic regions of castings LP3W, LP5W, HP3W, and HP5W is equal to 36.0% (±2.7%), 38.4% (±2.7%), 37.7% (±1.9%), 38.0% (±4.4%), respectively. It is visible that the increase in withdrawal rate led to a slight increase in $V_{f\gamma'}$. The higher withdrawal rate favors higher matrix saturation, and during the cooling a higher volume fraction of the γ' precipitates can re-precipitate. The mean size of the secondary γ' precipitates, expressed as the equivalent side of a square, was calculated to quantitatively analyze the differences originating from the influence of mold temperature, withdrawal rate and solution treatment. Histograms representing the secondary γ' precipitates' mean size, and curves describing their log-normal distribution, are shown in Fig. 6. In castings produced in shell molds preheated to 1510 °C (LP3W and LP5W) the increase in withdrawal rate from 3.4 to 5.0 mm/min led to the decrease in the secondary γ' precipitates mean size from 0.229 to 0.203 µm. In casting HP3W (V_s = 3.4 mm/min, T_0 = 1566 °C), the largest mean precipitate size of 0.250 µm was obtained. When the withdrawal rate was increased to 5.0 mm/min (HP5W), the mean secondary γ' precipitate size decreased to 0.263 µm. The size of the γ' precipitates is smaller than in the analogous variants of castings before solution heat treatment. In as-cast condition, the average precipitate size was 0.465 µm, 0.437 µm, 0.481 µm, and 0.457 µm for castings LP3W, LP5W, HP3W, and HP5W, respectively. SHT leads to partial dissolution of the γ' precipitates, which can be observed in the microstructure. After solution heat treatment, aging was performed to form the final morphology of the γ' precipitates and resultant properties. The influence of γ' phase size on the superalloy's strength is complex. In the event of obtaining precipitates below the critical size (border for the occurrence of the Orowan mechanism) dislocations could cut right through them. Additionally, γ' precipitate has an ordered $L1_2$ crystal structure, meaning that dislocations could cut or bypass the phase though various complex mechanisms, depending on the stress and service temperature. In the present experiment, the variable parameters were the withdrawal rate and mold preheating temperature, while solutioning conditions were constant for all casting variants. The higher preheating

Table 4 k^i coefficients of selected alloying elements calculated based on the SEM-EDX measurements

k^i Casting	k^{Ni}	k^{Co}	k^{Cr}	k^{W}	k^{Mo}	k^{Ti}	k^{Hf}	k^{Ta}	k^{Al}
LP3W	0.99 (±0.02)	1.00 (±0.03)	1.00 (±0.06)	1.11 (±0.15)	1.00 (±0.23)	0.91 (±0.16)	0.60 (±0.26)	1.00 (±0.09)	1.03 (±0.10)
LP5W	0.98 (±0.02)	0.99 (±0.03)	1.00 (±0.05)	1.11 (±0.15)	1.06 (±0.28)	0.90 (±0.15)	0.67 (±0.31)	1.00 (±0.08)	1.07 (±0.10)
HP3W	0.98 (±0.02)	1.01 (±0.04)	1.01 (±0.05)	1.11 (±0.09)	1.10 (±0.26)	0.90 (±0.15)	0.72 (±0.30)	0.99 (±0.06)	1.08 (±0.09)
HP5W	0.98 (±0.03)	1.02 (±0.03)	1.02 (±0.06)	1.17 (±0.16)	1.04 (±0.28)	0.88 (±0.19)	0.70 (±0.26)	1.00 (±0.11)	1.01 (±0.13)

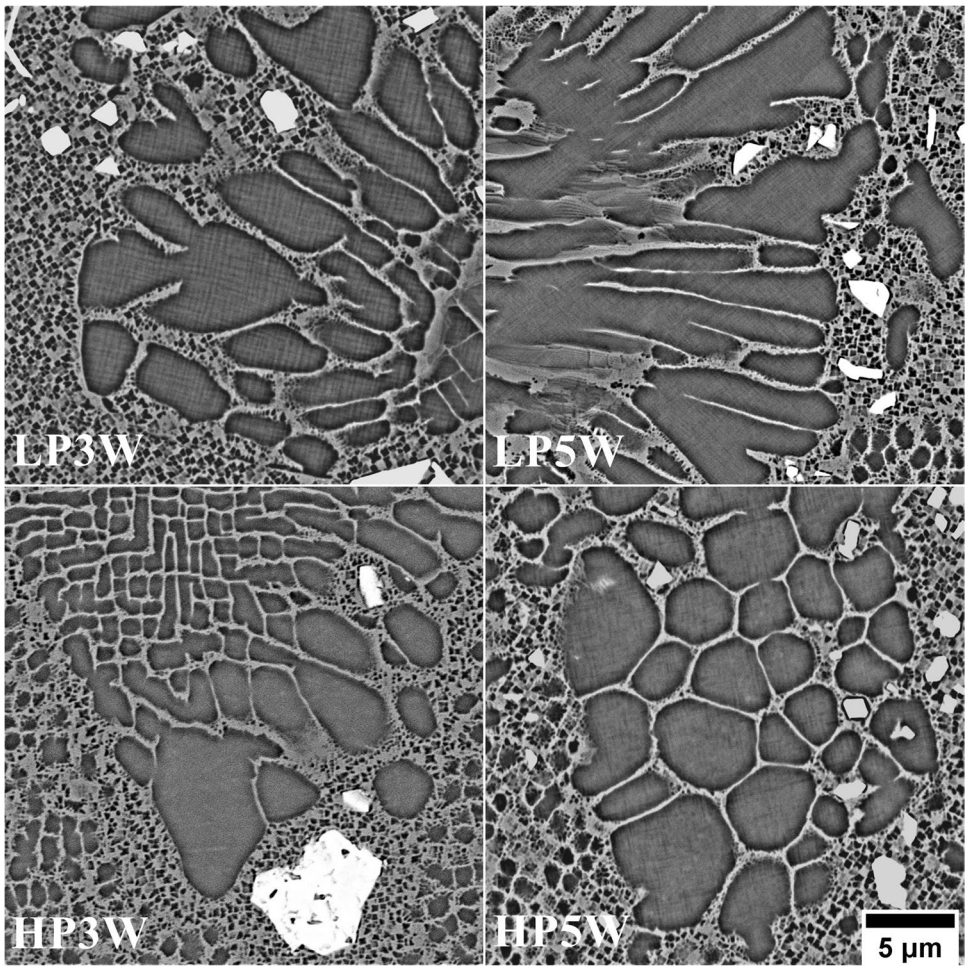

Fig. 4 Primary γ' precipitates morphology in DS MAR-M247 castings after SHT, SEM-BSE

Table 5 Results of semi-quantitative SEM-EDX analysis of the primary γ' precipitates

Casting/element	Ni	Al	Co	Cr	Ta	Ti	Mo	Hf	Ni/Al	(Ni, Co)/(Al, Ti, Ta, Hf)
1	65.3 (±0.6)	17.6 (±0.5)	7.0 (±0.1)	3.9 (±0.2)	2.7 (±0.2)	2.0 (±0.2)	0.4 (±0.1)	1.0 (±0.2)	3.7 (±0.1)	3.1 (±0.1)
2	64.7 (±0.8)	18.2 (±0.4)	7.0 (±0.3)	4.1 (±0.6)	2.7 (±0.2)	2.0 (±0.2)	0.4 (±0.2)	0.9 (±0.2)	3.6 (±0.1)	3.0 (±0.1)
3	64.6 (±0.8)	18.3 (±0.5)	7.0 (±0.1)	4.0 (±0.3)	2.7 (±0.2)	2.1 (±0.2)	0.4 (±0.2)	0.9 (±0.2)	3.5 (±0.1)	3.0 (±0.1)
4	64.4 (±0.9)	18.0 (±0.7)	7.0 (±0.4)	4.2 (±0.7)	3.0 (±0.3)	2.1 (±0.2)	0.5 (±0.2)	0.8 (±0.2)	3.6 (±0.2)	3.0 (±0.1)

temperature and lower withdrawal rate induced slower cooling rates, giving more time for γ' nuclei to re-precipitating and grow. Local thermodynamic conditions are determined by the chemical composition, state of elastic stresses, and the mutual interaction between precipitates. These factors change with temperature and are conditioned by the system's attempt to achieve thermodynamic equilibrium [25–28].

The secondary γ' precipitates located in interdendritic spaces are characterized by a more significant variation in size and more complex morphology (Fig. 5). Their shape deviated from cubic as a function of their size. Generally, the reduction of the system's internal energy drives microstructural evolution in complex alloys, such as Ni-based superalloys [25–27]. Equation (5) can express the energy state (E_{total}) of a single coherent γ' precipitate. It is widely accepted that minimizing the sum of elastic strain energy and surface energy determines the morphology of a single γ' precipitate.

$$E_{total} = E_{str} + E_{surf} + E_{int} \quad (5)$$

where E_{str} is the elastic strain energy caused by the lattice misfit between the γ' precipitate and γ matrix; E_{surf} is the

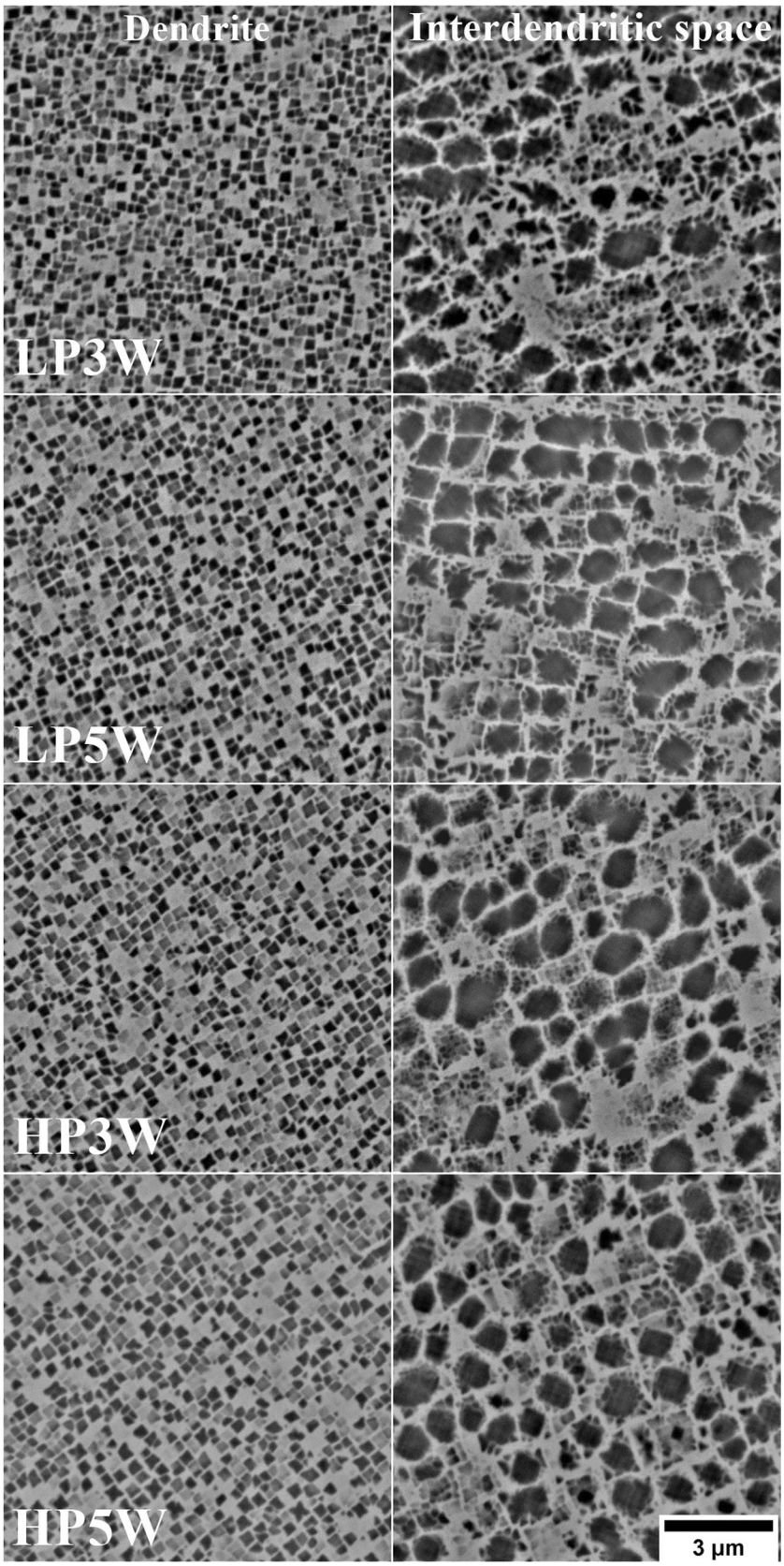

Fig. 5 Morphology of the secondary γ' precipitates in dendritic region and interdendritic spaces, SEM-BSE

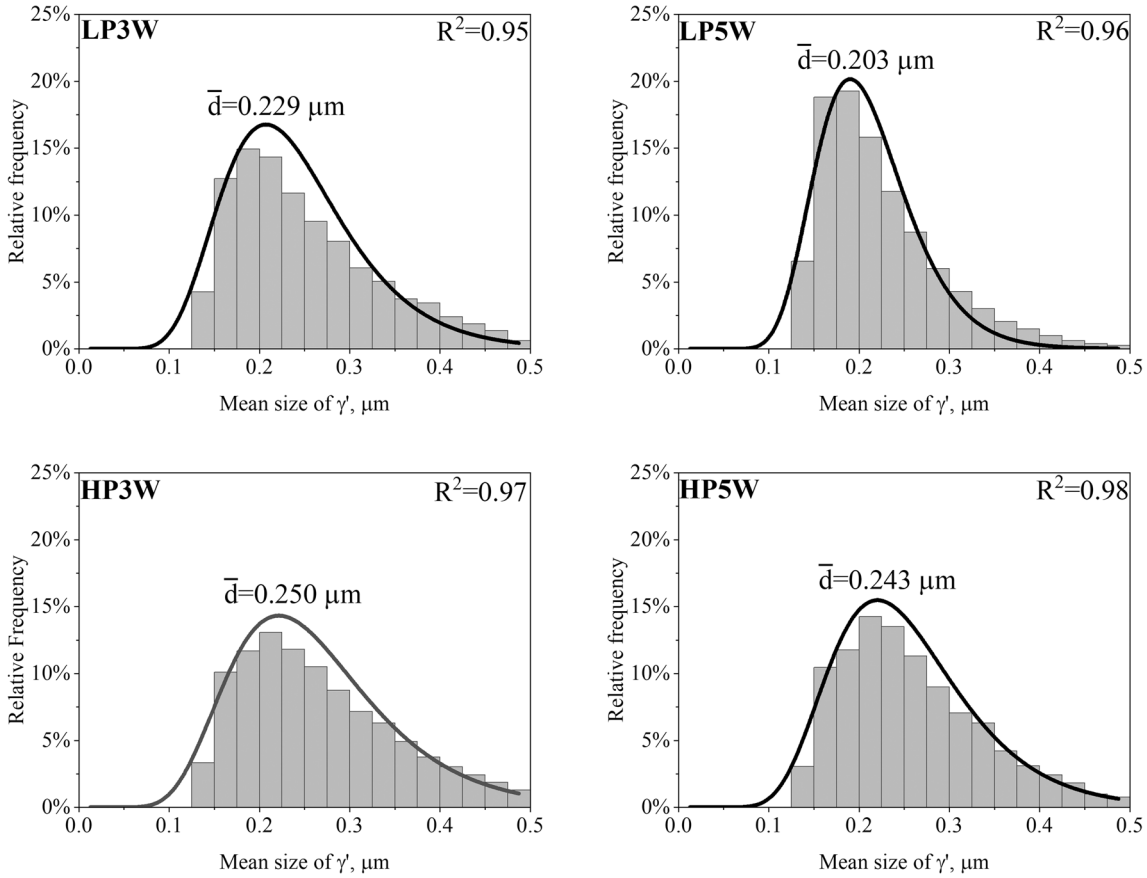

Fig. 6 Histogram of the secondary γ' precipitates in dendritic regions in DS MAR-M247 castings after SHT

surface energy (interfacial energy) of the γ' precipitate; and E_{int} is the elastic interaction energy between γ' precipitates.

Transformations following the order of sphere → cube → octocube morphology occur very quickly since an interfacial reaction controls the process. The atomic jump frequency through the interface is more critical than long-distance diffusion [28]. This process can occur via atom diffusion from one edge of γ' to another, filling the γ matrix. This causes the merger of two adjacent γ' phases, creating an elongated and/or irregular γ' phase in the process, as observed in the interdendritic spaces. For fine γ' phase precipitates, the interfacial energy is larger, bringing about a spherical or quasi-spherical morphology. However, as the γ' coarsens, the elastic energy contribution tends to dominate due to coherency loss [29]. Therefore, the γ' phase changes morphology from spherical to cubic. Considering the same heat-treatment procedure was carried out on all castings, the slower cooling rate in the directional solidification process could lead to a coarser solid-state cuboidal γ' directly before SHT. In the case of complex flower-like secondary γ' precipitates, they can easily become stress concentration sites for cavity nucleation and crack initiation due to their more significant curvature [30]. In turn, further growth of such precipitates is negligible. Their shape changes from complex flower-like to roughly cubical, which is advantageous for improved strength during exposure to elevated temperatures.

3.4 Morphology and chemical composition of MC carbides

The MAR-M247 superalloy contains alloying elements with high chemical affinity to carbon, i.e., Ta, Ti, Hf, and W. Under conditions of directional solidification, these elements tend to segregate, in turn creating favorable conditions for the precipitation of minor phases within interdendritic spaces (Fig. 7). These brightly contrasted precipitates (high *Z*-number) are MC-type carbides, characterized by various morphologies like simple blocks, sharp-edged parallelograms, or herringbone (Chinese Script) patterns. The V_f value for each casting is LP3W, 1.91% (±0.48%); LP5W, 1.86% (±0.25%); HP3W, 1.89% (±0.33%); HP5W, 1.87% (±0.45%). The data indicate that an increase in withdrawal rate can lead to a decrease in the carbide volume fraction. Carbide imaging was coupled with chemical composition analysis via SEM-EDX (example of point analysis location marked in Fig. 7), and the semi-quantitative results are

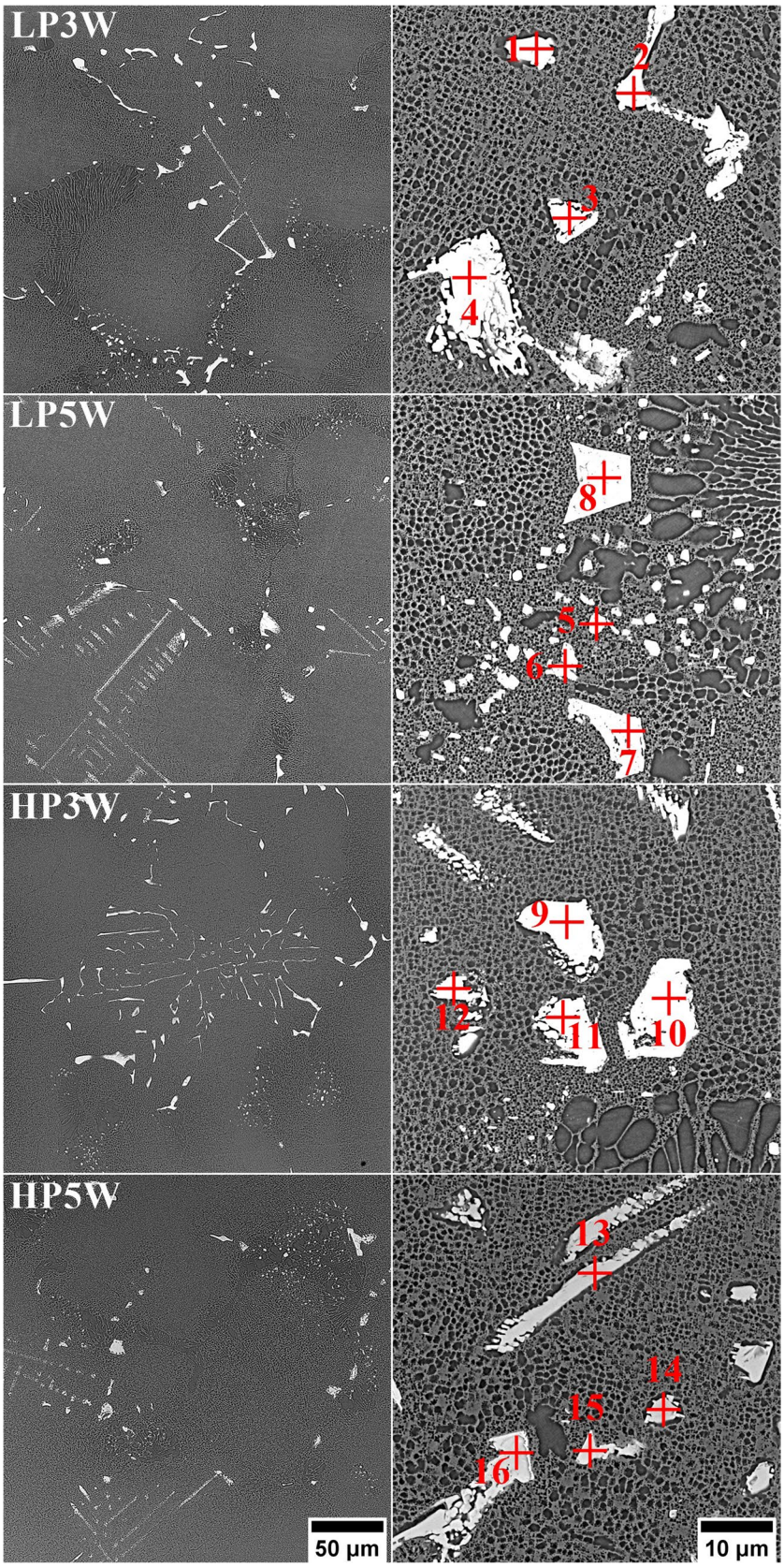

Fig. 7 Distribution and morphology of MC carbides in the DS MAR-M247 castings, SEM-BSE (EDX analysis points marked as red crosses)

presented in Table 6. Four points were measured for each selected carbide to evaluate the differences in the strong carbide-former concentrations throughout the fabricated castings. The carbides in casting LP3W mainly contained Ta and Ti, the sum of which exceeded 60 at%. W and Hf were also found, with their contents ranging from 6.8 to 11.9 at% and 6.4 to 14.5 at%, respectively. In contrast, the dominant carbide-former in casting LP5W was Hf, with measured concentrations spanning from 31.8 to 71.8 at%. The Hf-rich carbide is located closer to the γ-γ' eutectic island, indicating that it precipitated directly from the liquid phase early in the solidification stage. For points 5 and 6, Hf exceeded 65 at%, while the sum of W and Ti was less than 4 at%. Lower Hf concentrations were measured for points 7 and 8 (< 45 at%), with increased amounts of Ta, W, and Ti detected. Casting HP3W possessed carbides rich in Ta and Ti, while Hf ranged from 8.0 to 23.8 at% and W did not vary significantly. Points 13 and 14 of casting HP5W show that Ta and Ti are predominantly found in the MC carbides, similarly as points 1–4 in casting LP3W. The sum of Hf and W contents did not exceed 20 at%. Points 15 and 16 revealed greater concentrations of Hf and lower concentrations of Ta, W, and Ti, translating to a decrease in Ta/Hf. Similar MC carbide chemical composition relationships were found in ref. [23] for as-cast state, which may indicate high stability at high temperatures.

Based on the results of 80 measurements for each casting, it was observed that there are concentration relationships between strong carbide-formers, which can be presented as 3D graphs (Fig. 8). It is revealed that with a decrease in the concentration ratio (Ta + Hf)/(W + Ti), the concentration relationships (Ta/Hf)/(W + Ti) and Ta/Hf begin to increase.

The MC carbide morphology we observe is mainly affected by the production parameters. Ta promotes the formation of script-type MC carbides, whereas Hf is favorable for forming blocky shapes. The order of carbide formation from difficult to easy is as follows: WC, ZrC, TaC, TiC, HfC. Hf is a popular alloying element in DS Ni-based superalloys as it can decrease susceptibility to hot cracking; however, it forms stable carbides already during solidification. The standard Gibbs energies of formation of MC carbides at 1250 °C are HfC ($\Delta_f G^0 = -48.1$ kcal/mol), TaC ($\Delta_f G^0 = -33.6$ kcal/mol), TiC ($\Delta_f G^0 = -39.7$ kcal/mol), and WC ($\Delta_f G^0 = -8.3$ kcal/mol), where HfC has the greatest stability [16]. Carbides crystallizing in the same crystallographic system can mutually dissolve in each other [31]. Murata [32] showed that Ta and Nb additions to Inconel 100 changed the MC-type TiC carbides' composition. Nb, Ta, and Ti have similar metallic radii, which facilitate Ta and Nb replacing Ti in the metallic site of MCs, reducing the Gibbs energy. Mo and W have lower solubility, as their metallic radii are larger. Therefore, it is possible that Hf's lower concentration in the studied MC carbides possessing complex morphologies is due to its larger atomic radius (compared to Ta and Ti), as well as its lower diffusivity in liquid. The casting solidification rate significantly affected carbide morphology and distribution. Under near-equilibrium conditions, the MC carbides assume block shapes with sharp edges, whereas under non-equilibrium conditions they take on more complex shapes, e.g., the herringbone-like pattern (a.k.a.

Table 6 The results of semi-quantitative SEM-EDX analysis of MC carbides

Casting	Element point	Ni	Co	Cr	Ta	W	Ti	Mo	Hf	Ta/Hf	(Ta + Hf)/(W + Ti)	(Ta/Hf)/(W + Ti)
LP3W	1	8.3	1.7	2.1	38.8	9.9	28.6	2.9	7.6	5.09	1.20	0.132
	2	7.2	1.5	2.4	38.5	11.9	29.6	2.5	6.4	6.04	1.08	0.146
	3	9.8	2.9	2.5	36.0	6.8	25.6	1.9	14.5	2.48	1.56	0.077
	4	6.4	2.1	2.1	39.3	8.6	27.6	2.2	11.8	3.33	1.41	0.092
LP5W	5	12.3	2.3	2.5	6.2	1.2	2.3	1.3	71.8	0.09	22.37	0.025
	6	12.7	2.8	2.2	8.3	1.3	2.1	1.8	68.7	0.12	22.46	0.035
	7	9.1	3.0	2.2	22.9	5.8	11.0	1.6	44.5	0.51	4.01	0.031
	8	7.5	2.6	1.8	31.3	5.7	17.1	2.1	31.8	0.98	2.77	0.043
HP3W	9	6.3	1.7	0.8	35.9	6.2	22.9	2.5	23.8	1.51	2.05	0.052
	10	7.0	1.5	1.3	40.3	7.8	29.8	2.3	10.0	4.05	1.34	0.108
	11	7.8	1.6	1.3	36.8	6.7	25.2	2.1	18.7	1.97	1.75	0.062
	12	8.4	2.4	2.2	38.5	9.7	28.5	2.3	8.0	4.81	1.22	0.126
HP5W	13	9.1	2.5	3.0	36.7	10.9	27.6	2.5	7.8	4.71	1.16	0.122
	14	8.7	3.2	3.3	35.6	9.9	26.9	2.6	9.9	3.59	1.24	0.098
	15	9.9	3.3	2.2	20.7	5.8	9.6	1.5	47.1	0.44	4.41	0.029
	16	7.6	1.7	1.2	28.3	5.6	13.4	1.0	41.1	0.69	3.64	0.036

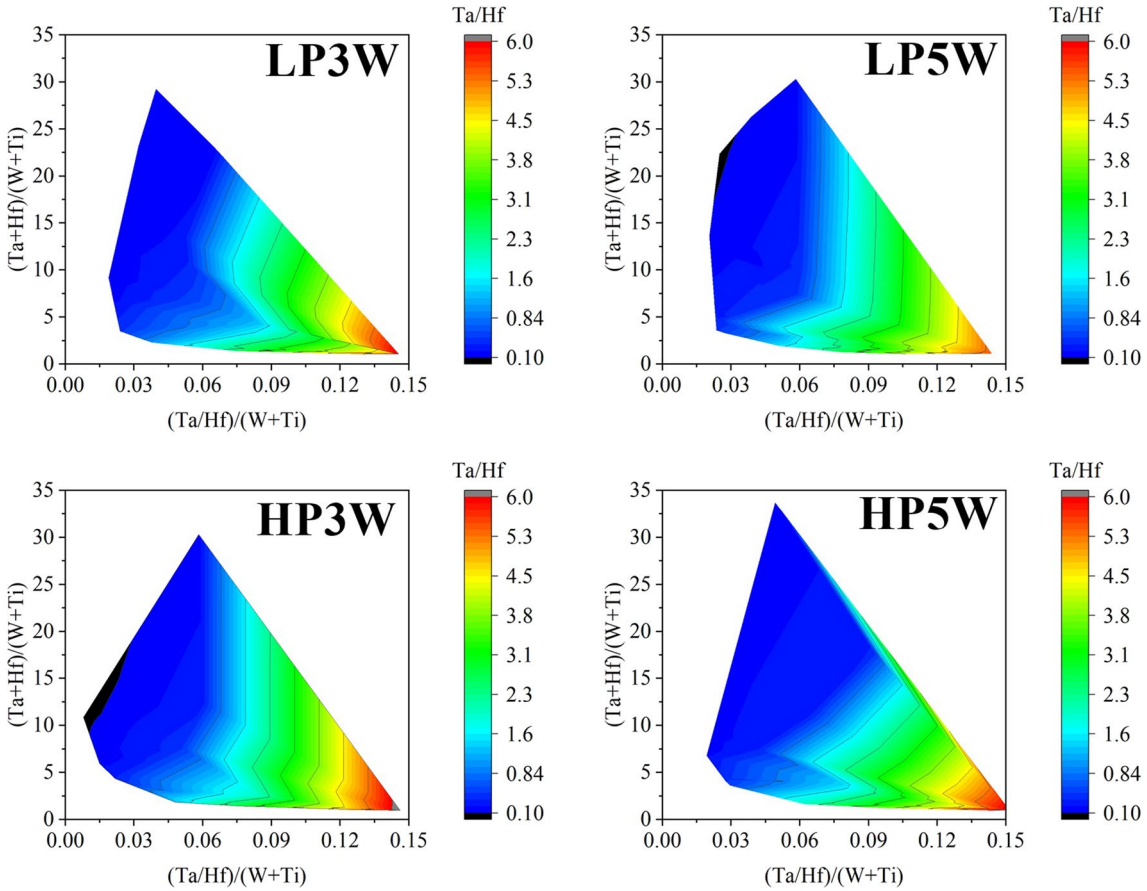

Fig. 8 MC carbide concentration relationships Ta/Hf, (Ta + Hf)/(W + Ti) and (Ta/Hf)/(W + Ti) calculated based on semi-quantitative SEM-EDX results

Chinese script). Other carbide types, e.g., M_3C_2, were not found, which might be related to the high SHT temperature. However, this does not mean that the observed carbides will be stable during aging and subsequent usage, despite their high melting temperature. The concentration of Ta and Hf in the MC carbides influences their behavior during subsequent aging and high temperature servicing. Aged Renè 108, characterized by a similar chemical composition as DS MAR-M247, predominantly contains MC-type carbides. On the edges of herringbone-shaped carbides (Ta-rich), $M_{23}C_6$ nano-carbides were found via HAADF-STEM [24]. Long-term service or aging/annealing can lead to the transformation of MC carbides into more stable $M_{23}C_6$ or M_6C carbides, with a lower carbon concentration, according to the widely known phase transformations [33]: MC + $\gamma \rightarrow M_{23}C_6 + \gamma'$ (I); MC + $\gamma \rightarrow M_{23}C_6 + \eta$ (II); MC + $\gamma \rightarrow M_6C + \gamma'$ (III). $M_{23}C_6$ forms through phase transformation (I), as MC degradation did not accompany the formation of η due to low initial Ti concentration within the material. ThermoCalc simulations indicate that this phase transformation can occur in DS MAR-M247 below 1010 °C, suggesting that it can be initiated during subsequent ageing. As observed in Renè 108, MC carbides with a blocky-like morphology and dominant Hf concentration did not degrade according to the abovementioned reactions. A similar conclusion was stated by Li [30], who observed that Hf-rich blocky MC carbides exhibit excellent stability. In contrast, Ta-rich herringbone-like carbides gradually degenerate with $M_{23}C_6$ thin film formation at 800 °C, which is in line with our thermodynamic calculations. By studying the effect of temperature on the homogenization of the liquid Ni-based superalloy Inconel 738LC, Liu [34] showed that MC carbides could be present at temperatures exceeding the liquidus. At approx. 1550 °C, MC carbides dissolve entirely in the liquid after only 5–10 min. For comparison, the liquidus temperature of the Inconel 738LC superalloy is lower (1336–1342 °C). M_3C_2 carbides and the $Ni_7(Hf, Zr)_2$ intermetallic phase can also occur in the interdendritic spaces of as-cast DS MAR-M247 [23]. After heat treatment, M_3C_2 and $Ni_7(Hf, Zr)_2$ were not detected, which suggests their complete dissolution in the γ phase. Thermodynamic simulations also do not predict these phases to be present at elevated temperatures. The $Ni_7(Hf,$

$Zr)_2$ phase undergoes a phase transformation MC + (Ni, $Co)_7(Hf, Zr)_2$ + Cr (in the matrix) → (Hf, Zr)C + $Cr_{23}C_6$ + γ [32]. $Ni_7(X)_2$ precipitates have been observed both in superalloys with the addition of Hf, such as MAR-M004, and in the Hf-free Inconel 713C [35, 36]. Hf-rich blocky-shaped secondary MC carbides, precipitated during SHT, were found in the interdendritic spaces, confirmed via SEM-EDX distribution maps (Fig. 9). Precipitates with a bright phase contrast are observed on the castings' grain boundaries, forming both continuous and discontinuous patterns. SEM-EDX point analysis was performed (Fig. 10) and the results (Table 7) revealed that these precipitates are enriched in W and Cr.

Based on XRD results and as-cast DS MAR-M247 analysis [23], it can be concluded that these are M_5B_3 borides. The addition of boron can have a significant impact on grain boundary precipitation in Ni-based superalloys. In these alloys, boron atoms are larger than interstitial atoms but smaller than substitutional atoms, resulting in considerable lattice distortion. Boron, due to its small diameter, can fill vacancies at grain boundaries and reduce diffusivity in these regions [37]. From an energetic perspective, it is beneficial for B to be in areas with less-dense atom packing, such as grain and interfacial boundaries. However, the solubility of boron in alloys with a face-centered cubic lattice is very low, resulting in significant segregation during casting and the precipitation of borides with reaching several tens of micrometers. This can increase the risk of incipient melting during SHT. In superalloys, such as Inconel 738 and Renè 80, the precipitation of borides occurred when the B concentration was 0.06 %at and 0.065 %at, respectively. In contrast, borides did not form in superalloys, such as Inconel 617B and 263, where the B concentration was

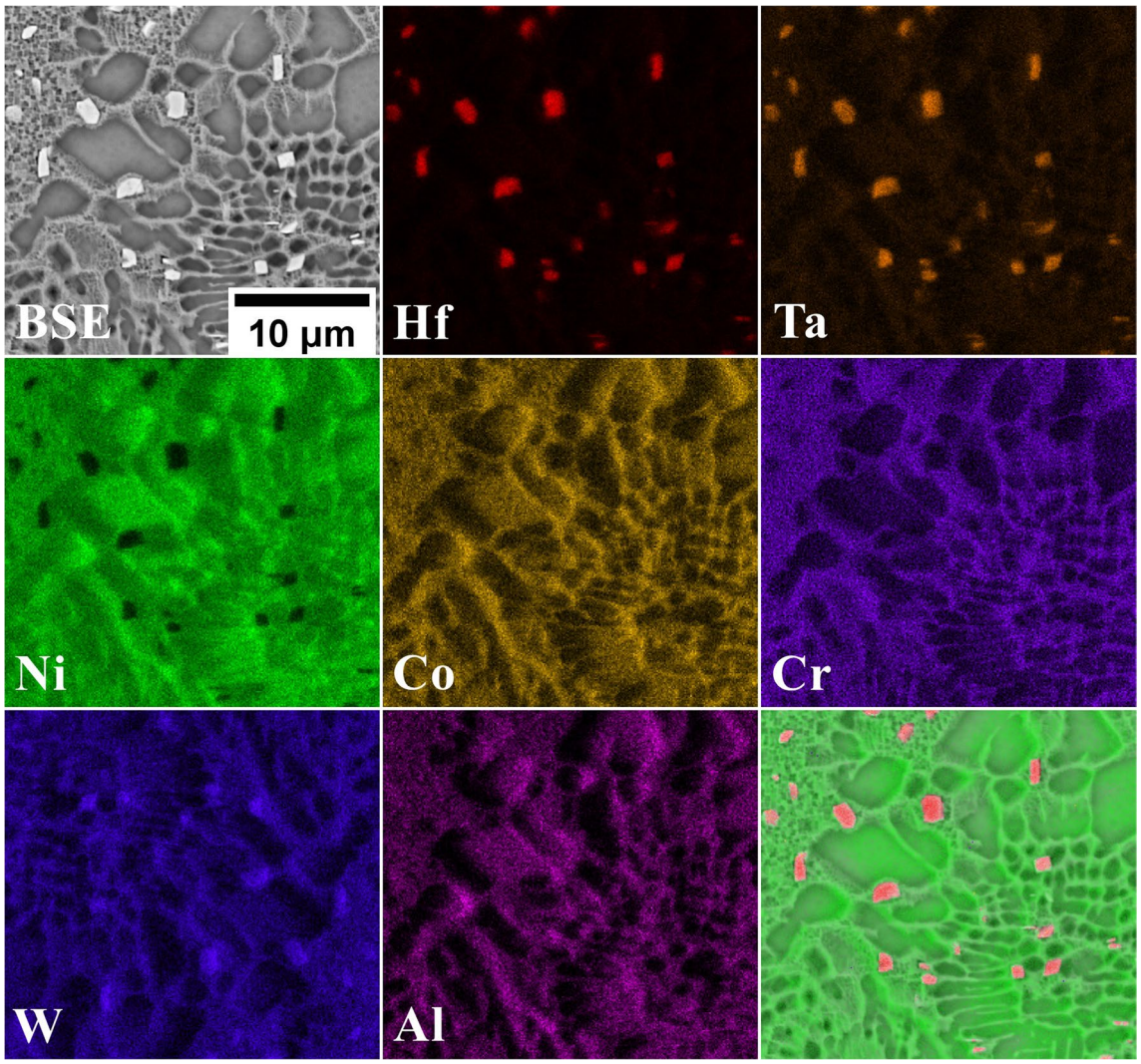

Fig. 9 Alloying element distribution maps of secondary MC carbides, SEM-EDX

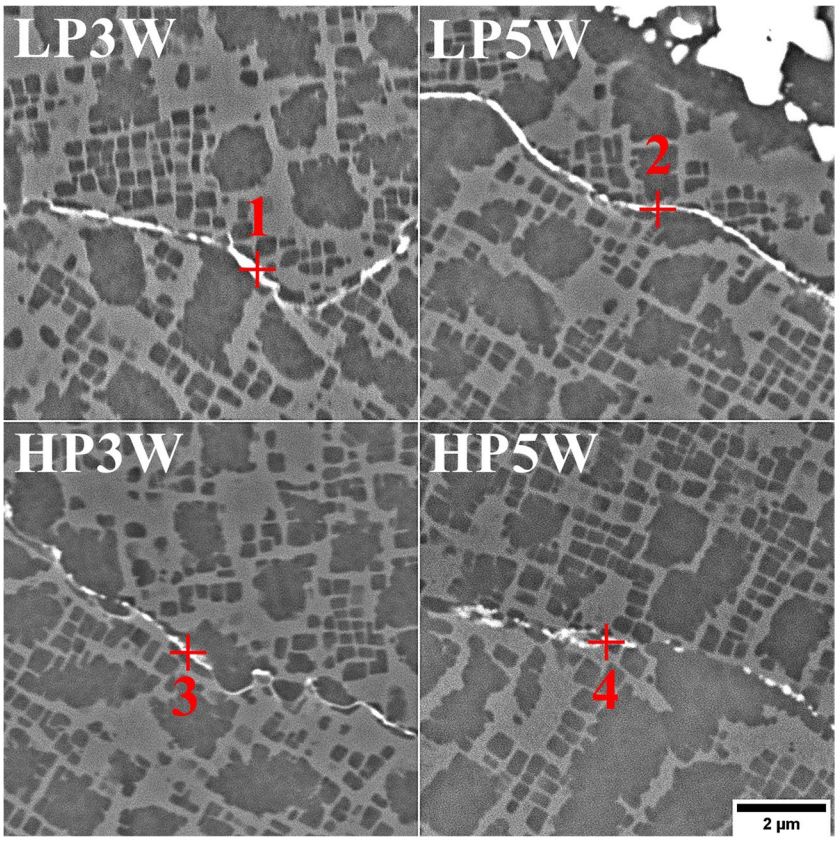

Fig. 10 The M_5B_3 borides in the DS MAR-M247 castings, SEM-BSE

Table 7 Semi-quantitative SEM-EDX analysis results of the precipitates along grain boundaries, at%

Casting	Point	Ni	W	Cr	Al	Co	Ta	Mo	Ti	Hf
LP3W	1	47.8	14.6	12.4	11.2	7.3	2.8	2.5	1.4	0.1
LP5W	2	49.5	12.2	11.3	12.3	7.6	3.3	2.4	1.2	0.2
HP3W	3	47.4	15.8	14.7	9.0	7.0	2.2	2.5	1.1	0.1
HP5W	4	45.6	12.0	13.5	11.4	10.3	3.0	3.0	1.1	0.3

lower (0.02 at% and 0.015 at%, respectively) [38, 39]. As the intermetallic γ' phase forms, W, Cr, and Mo are more likely to dissolve in the γ matrix and be expelled to the γ/γ' interfaces, where they interact with B atoms to form borides. The formation of these borides at grain boundaries pins them and impedes the grain-boundary sliding mechanism at high temperatures. Xiao [38] suggested that strong interaction between B atoms and dislocation cores could hinder dislocation motion, increasing resistance to fatigue failure.

3.5 Characterization of the mechanical properties of DS MAR-M247 castings

The mechanical properties of the DS MAR-M247 castings were determined via tensile tests at room temperature. Based on the obtained curves (Fig. 11), it can be

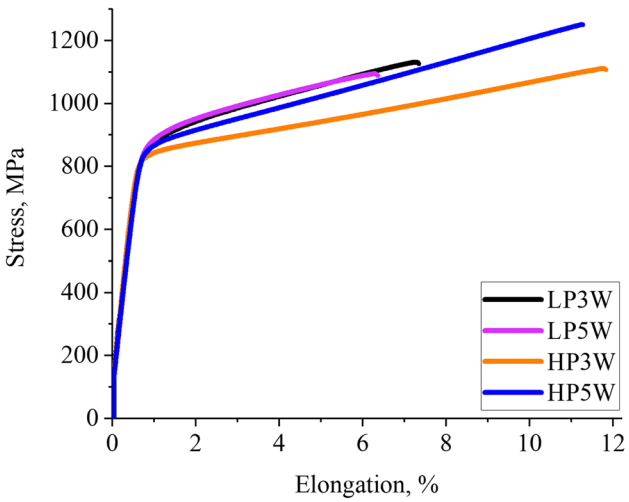

Fig. 11 Tensile test curves of the DS MAR-M247 castings after SHT

Table 8 Summary of DS MAR-M247 castings' mechanical properties

Casting	Elongation, %	Yield point, MPa	Tensile strength, MPa
LP3W	7.4	834	1130
LP5W	6.4	830	1094
HP3W	12.0	800	1111
HP5W	11.4	818	1250

observed that castings produced at a higher temperatures and withdrawal rate possessed greater elongation. The castings' elongation, yield point and tensile strength are summarized in Table 8. Based on specification EMS-55447 [21], the minimum required yield and ultimate tensile strength for the MAR-M247 castings are 725 MPa and 966 MPa, respectively. The obtained results indicate that the selected parameters enable the production of castings with sufficiently high strength. Huang [40], based on the tensile test results of fully heat-treated CM-247LC castings (like MAR-M247), observed that fine-grain test bars (80−90 µm) have a higher yield strength and higher elongation than those of coarse grains (2–3 mm). For fine-grained samples, the obtained values were UTS = 1242 MPa, YS = 1010 MPa, and $E = 8.1\%$, whereas for the coarse-grained ones they were UTS = 1069 MPa, YS = 939 MPa, and $E = 5.7\%$. Intermediate values of UTS = 1192 MPa, YS = 985 MPa, and $E = 7.2\%$ were obtained for the 200–300 µm grain size variant.

The high-volume fraction of γ' precipitates gives the superalloy its desirable strength. A further increase in mechanical properties originates from γ solution strengthening and the precipitation of MC carbides and borides. In the matrix, deformation occurs by dislocation slip in the {111}<110> systems and at elevate temperatures via transverse dislocation slipping and climbing. The γ' precipitates deform also through dislocation slipping in the {111}<110> systems. There, the Burgers vector of the total dislocation has a length of $(a\sqrt{2})$, which is twice as long as in the matrix. Therefore, complete dislocation slipping from γ to γ' phase is impossible without the formation of a high-energy antiphase boundary defect. The doubled length of the γ' phase's dislocation vector originates from its 4-times greater energy in comparison to γ. To reduce this energy, superpartial dislocations (characterized by shorter Burgers vectors, a/2<101>) would need to form. In turn, these dislocations, connected by an antiphase boundary, would travel in pairs (superdislocations) through the γ' phase. They tend to change from {111} to {100} by transverse slipping [41–43]. The appearance of dislocation anchor points accompanies this change, the number of which increases with increasing temperature, and resulting in increased strength of the γ' phase [44]. At 700–900 °C, Ni-based superalloys with a γ' precipitate volume fraction of γ' precipitates of at least 40% showed increased yield point values, which is related to the deformation mechanism of the ordered γ' phase [45]. Similar behavior can be expected during service at high temperatures of the heat-treated DS MAR-M247 superalloy.

Selected images of sample fractures are presented in Fig. 11. The complex nature of the sample cracking was observed in all castings, with the main feature being dimples and cleavage surfaces at the fracture surfaces (Fig. 12a). Moreover, cracks occurred along the grain boundaries. It can be inferred that the fracture model is intergranular due to the lower strength of the grain boundaries. Brittle fractures are observed in MC carbides and γ-γ' eutectics (Fig. 12b, c). Large carbides, characterized by high hardness and brittleness, have numerous secondary cracks with pronounced edges, indicating no plastic deformation. During tensile tests, the MC carbide interface cannot be accommodated by gliding, the precipitates do not deform, resulting in a buildup of dislocations around them. The castings exhibited relatively low elongation, while increasing strain at the interfaces led to crack formation and their continuous propagation. The fracture surfaces display script-like cracks on the MC carbide/matrix interfaces, while the γ matrix channels exhibit considerable plastic deformation. Due to the substantial segregation of carbides and eutectic islands into the interdendritic spaces, a greater number of dimples can be observed in dendrite cores and arms, indicating matrix plastic deformation (Fig. 12d). This is attributed only to fine γ' precipitates surrounded by channels of the deformable matrix in those areas.

Figure 13 illustrates the microstructure of the fractures' cross-section, revealing various features. Numerous MC carbide and γ-γ' eutectic precipitations on the edges can be observed, suggesting crack initiation and propagation through the interdendritic spaces. No oxides or other nonmetallic inclusions on the fracture edges were identified; however, local secondary γ' precipitate deformation was registered. Secondary cracks were found near the carbides at a distance from the main fracture. The carbides play a crucial role in either hindering or promoting the initiation and propagation of intergranular cracks. They can affect the strength of grain boundaries and significantly impact the material's mechanical properties. Cracks tend to originate more readily along grain boundaries parallel to the major stress axes.

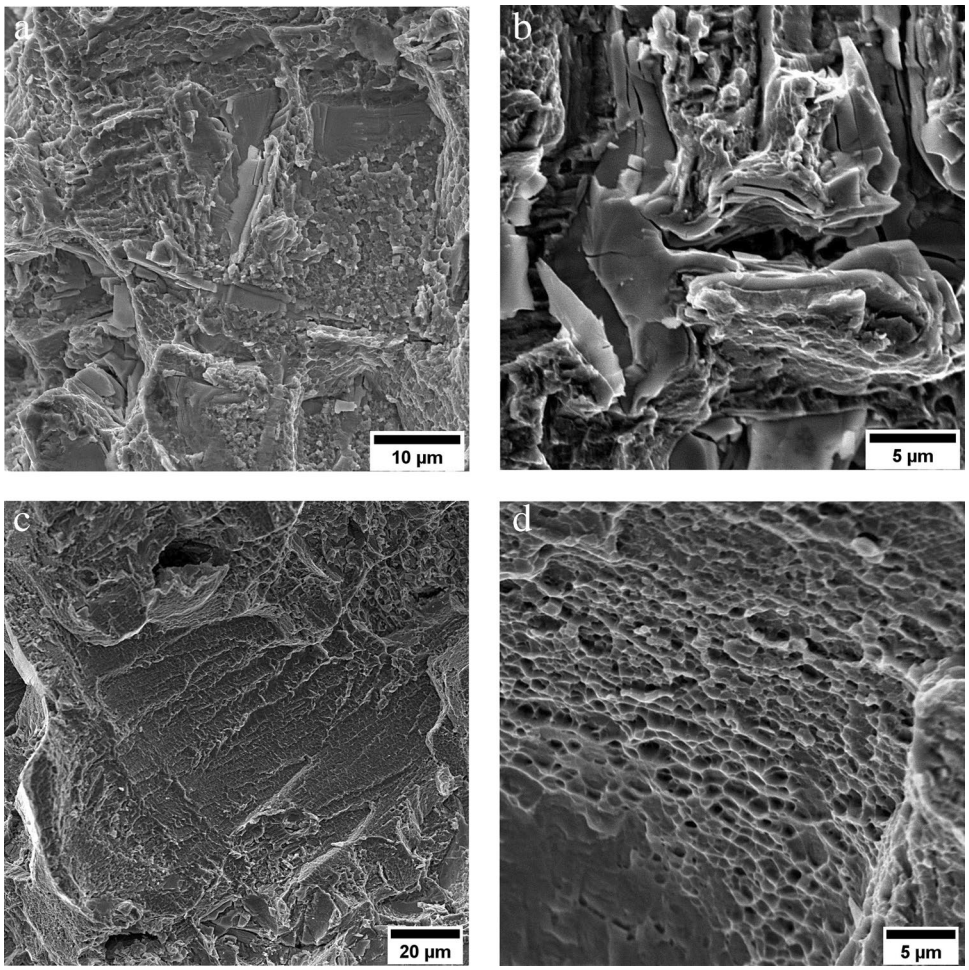

Fig. 12 Selected fracture images: **a** brittle fracture of carbides; **b** secondary fracture of carbides; **c** plastic deformation of the matrix in the area of eutectic γ-γ'; **d** plastic deformation (dimples) of the matrix in the dendritic region, SEM-SE

4 Conclusions

In this paper the microstructure and properties of the solution heat-treated DS MAR-M247 superalloy produced using different withdrawal rates (3.4 or 5.0 mm/min) and shell mold temperatures (1510 or 1566 °C) was analyzed. Based on the obtained results, the following conclusions can be drawn:

(1) The presence of γ, γ', MC carbides and M_5B_3 borides was confirmed in each casting variant via XRD.
(2) The volume fraction of the secondary γ' precipitates in the dendritic regions increased with increasing withdrawal rate. For a shell mold temperature of 1510 °C, the value changed from 36.0 to 38.4% and for 1566 °C from 37.7 to 38.0%.
(3) The increase in withdrawal rate during directional solidification led to a decrease in the mean size of secondary γ' precipitates in the dendritic regions. In castings LP3W and LP5W, the mean size of the secondary γ' precipitates decreased from 0.229 to 0.229 µm. For castings produced using a shell mold temperature of 1566 °C, the size changed from 0.250 µm (HP3W) to 0.243 µm (HP5W).
(4) The fraction of MC carbides slightly decreased with increasing withdrawal rate, i.e., from 1.92 to 1.86 pct for T_0 = 1510 °C and from 1.89 to 1.87 pct for T_0 = 1566 °C.
(5) The castings produced with a shell mold temperature of 1566 °C were characterized by higher elongation (min. 11%).

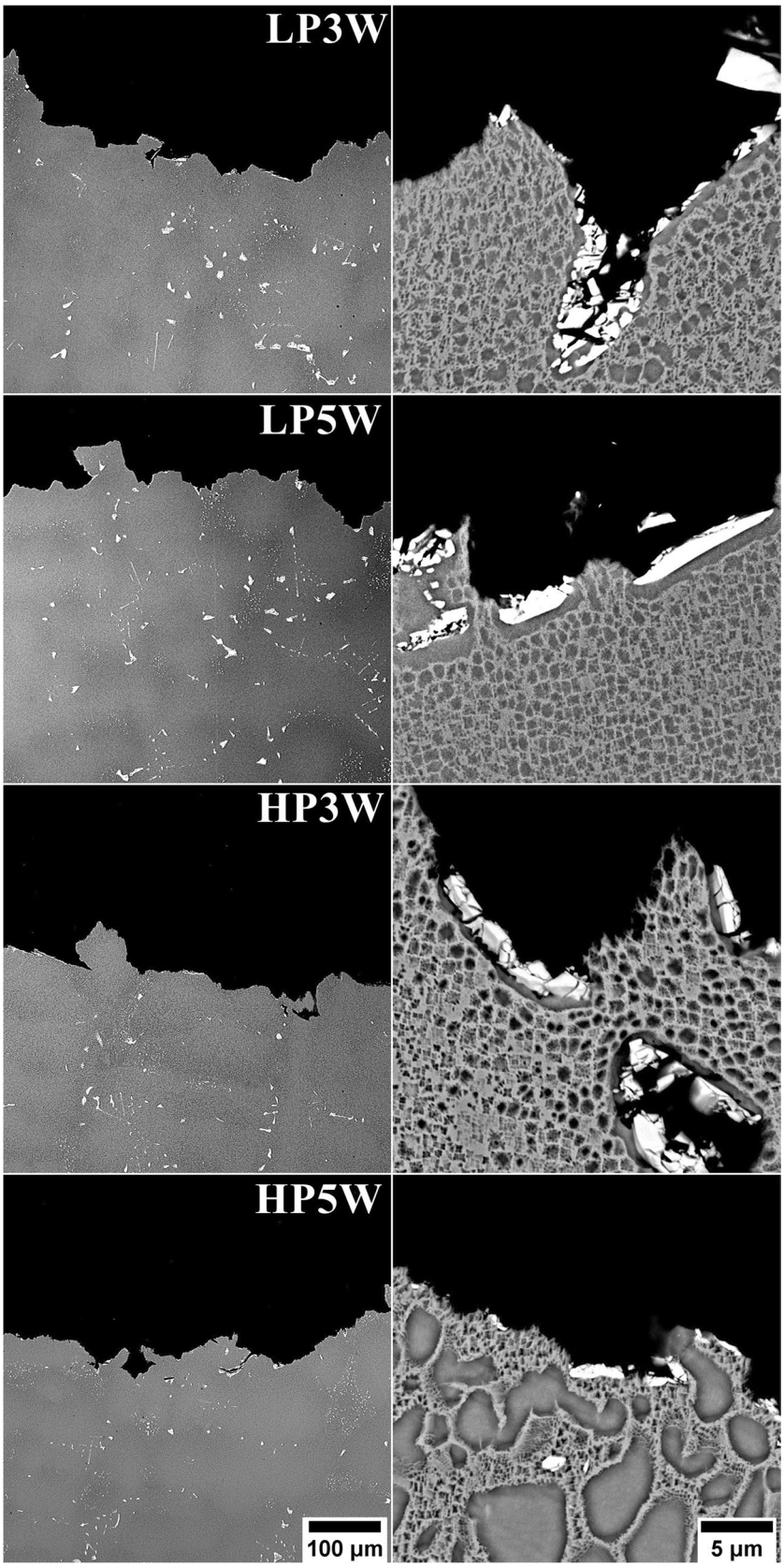

Fig. 13 Morphology of the cross-sectioned tensile test fractures of DS MAR-M247 castings, SEM-BSE

Author contributions ŁR wrote the original draft and performed the experiments. MGR carried out the fractography analysis and edited the original draft. RC prepared materials for experiments and was responsible for project management. TK performed and analyzed differential scanning calorimetry results. AZL reviewed and edited the original draft.

Funding The authors gratefully acknowledge the funding by National Centre for Research and Development, Poland, under grant POIR.01.01.01-00-1335/20. ŁR would also like to thank the Polish Ministry of Science and Higher Education (subvention AGH no. 16.16.110.663) for its financial support.

Declarations

Ethical approval This article does not contain any studies with human participants or animals performed by any of the authors.

Conflict of interest The authors declare no competing interests.

References

1. Reed RC (2006) The superalloys: fundamentals and applications. Cambridge University Press, Cambridge
2. Sims C, Stoloff NS, Hagel WC (1987) Superalloys II: high-temperature materials for aerospace and industrial power. John Wiley & Sons, New York
3. Harte A, Atkinson M, Smith A, Drouven C, Zaefferer S, da Fonseca JQ, Preuss M (2020) The effect of solid solution and gamma prime on the deformation modes in Ni-based superalloys. Act Mat 194:257–275. https://doi.org/10.1016/j.actamat.2020.04.004
4. Thebaud L, Villechaise P, Crozet C, Devaux A, Bechet D, Franchet JM, Rouffie AL, Mills M, Cormier J (2018) Is there an optimal grain size for creep resistance in Ni-based disk superalloys? Mat Sci Eng A 716:274–283. https://doi.org/10.1016/j.msea.2017.12.104
5. Ali MA, Lopez-Galilea I, Gao S, Ruttert B, Amin W, Shchyglo O, Hartmaier A, Theisen W, Steinbach I (2020) Effect of γ′ precipitate size on hardness and creep properties of Ni-base single crystal superalloys: experiment and simulation. Mater 12:100692. https://doi.org/10.1016/j.mtla.2020.100692
6. Strutt VCI, Jenkins BM, Woolrich JM, Appleton M, Moody MP, Bagot PAJ (2023) Effect of microsegregation and heat treatment on localised γ and γ' compositions in single crystal Ni-based superalloys. J All Comp 949:169861. https://doi.org/10.1016/j.jallcom.2023.169861
7. Kim DM, Kim C, Yang CH, Park JU, Jeong HW, Yim KH, Hong HU (2023) Heat treatment design of Inconel 740H superalloy for microstructure stability and enhanced creep properties. J All Comp 946:169341. https://doi.org/10.1016/j.jallcom.2023.169341
8. Geranmayeh A, Malekan M, Forghani F, Ghorbani H (2023) Microstructural and mechanical investigations on the heat treatment rejuvenation of a long-term service-exposed GTD-111 Ni-based superalloy. Mat Sci Eng A 862:144381. https://doi.org/10.1016/j.msea.2022.144381
9. Szeliga D, Motyka M, Ziaja W, Cygan R, Fuglewicz S, Gromada M (2023) Study of solidification process of Ni-based superalloy castings manufactured in industrial conditions with the use of novel thermal insulating module technique. JOM 75(6):2034–2044. https://doi.org/10.1007/s11837-023-05733-6
10. Masoumi F, Jahazi M, Shahriari D, Cormier J (2016) Coarsening and dissolution of γ′ precipitates during solution treatment of AD730™ Ni-based superalloy: mechanisms and kinetics models. J All Comp 658:981–995. https://doi.org/10.1016/j.jallcom.2015.11.002
11. Maciąg T, Migas D, Płachta A (2022) Experimental confirmation of high-temperature phase boundaries in the nickel-rich part of Ni-Al-Cr system. Arch Civ Mech Eng 22:203. https://doi.org/10.1007/s43452-022-00532-3
12. Xu J, Schulz F, Peng RL, Hryha E, Moverare (2021) Effect of heat treatment on the microstructure characteristics and microhardness of a novel γ′ nickel-based superalloy by laser powder bed fusion. Res Mat 12:100232. https://doi.org/10.1016/j.rinma.2021.100232
13. Lopez-Galilea I, Hecker L, Epishin A, Burger D, Ruttert B, Thome P, Weber S, Theisen W (2023) Super-solidus hot isostatic pressing heat treatments for advanced single crystal Ni-base superalloys. Metall Mat Trans A 54:1509–1525. https://doi.org/10.1007/s11661-022-06884-y
14. Tan YG, ·Liu F, Zhang AW, Han DW, Yao XY, Zhang WW, Sun WR (2019) Element segregation and solidification behavior of a Nb, Ti, Al co-strengthened superalloy ЭК151. Acta Metall Sin (Eng Lett) 32:1298–1308. https://doi.org/10.1007/s40195-019-00894-3
15. Wang H, Long H, Liu Y, Zhao Y, Li X, Yang G, Yang X, Chen Y, Mao S, Zhang Z, Han X (2023) The widening of the solution heat treatment window by the addition of Ru in Ni-based single crystal superalloy. Mat Char 203:113057. https://doi.org/10.1016/j.matchar.2023.113057
16. Baldan R, da Rocha RLP, Tomasiello RB, Nunes CA, da Silva Costa AM, Barboza MJR, Coelho GC, Rosenthal R (2013) Solutioning and aging of MAR-M247 nickel-based superalloy. J Mater Eng Perform 22:2574–2579. https://doi.org/10.1007/s11665-013-0565-4
17. e Silva PRSA, Baldan R, Nunes CA, Coelho GC, da Silva Costa AM (2013) Solution heat-treatment of Nb-modified MAR-M247 superalloy. Mat Char 75:214–219. https://doi.org/10.1016/j.matchar.2012.11.006
18. Salwan GK, Subbarao R, Mondal S (2021) Comparison and selection of suitable materials applicable for gas turbine blades. Mat Today: Proc 46(17):8864–8870. https://doi.org/10.1016/j.matpr.2021.05.003
19. Costa AMS, Lopes ESN, Contieri RJ, Caram R, Baldan R, Fuchs GE, Nunes CA (2019) Microstructural and mechanical characterization of directionally solidified conventional and Nb-modified Mar-M247 superalloy. J Mat Eng Perform 28(4):2427–2438. https://doi.org/10.1007/s11665-019-04014-1
20. Bor HY, Wei CN, Yeh AC, He WB, Wang HS, Kuo CM Heat treatment effects on the high temperature mechanical behavior of directionally solidified MAR- M247 superalloy. In: Proc. 8th Pacific Rim International Congress on Advanced Materials and Processing, pp 379–386. https://doi.org/10.1007/978-3-319-48764-9_46
21. Allied-Signal Aerospace Company. Engine materials specification 55447 (Castings, Investment, MAR-M247); 1988
22. Dahmen T, Henriksen NG, Dahl KV, Lapina A, Pedersen DB, Hattel JH, Christiansen TL, Somers MAJ (2021) Densification, microstructure, and mechanical properties of heat-treated MAR-M247 fabricated by binder jetting. Add Manuf 39:101912. https://doi.org/10.1016/j.addma.2021.101912
23. Rakoczy Ł, Grudzień-Rakoczy M, Cygan R, Kargul T, Maj Ł, Zielińska-Lipiec A (2023) Analysis of the as-cast microstructure and properties of the Ni-based superalloy Mar-M247®

produced via directional solidification. Metall Mater Trans A 54:3630–3652. https://doi.org/10.1007/s11661-023-07123-8
24. Rakoczy Ł, Rutkowski B, Grudzień M, Cygan R, Ratuszek W, Zielińska-Lipiec A (2020) Analysis of γ′ precipitates, carbides and nano-borides in heat-treated Ni-based superalloy using SEM, STEM-EDX, and HRSTEM. Mater 13(19):4452. https://doi.org/10.3390/ma13194452
25. Vogel F, Wanderka N, Balogh Z, Ibrahim M, Stender P, Schmitz G, Banhart J (2013) Mapping the evolution of hierarchical microstructures in a Ni-based superalloy. Nature Comm. 4:2955. https://doi.org/10.1038/ncomms3955
26. Zhang J, Lu F, Zhang C, Zhao Q, Huang T, Wang D, Zhang J, Zhang J, Su H, Liu L (2022) On the tungsten segregation at γ/γ′ interface in a Ni-based single-crystal superalloy. Vacuum 197:110863. https://doi.org/10.1016/j.vacuum.2021.110863
27. Xu J, Zhao X, Yue Q, Xia W, Duan H, Gu Y, Zhang Z (2023) A morphological control strategy of γ′ precipitates in nickel-based single-crystal superalloys: an aging design, fundamental principle, and evolutionary simulation. Mat Tod Nano 22:100335. https://doi.org/10.1016/j.mtnano.2023.100335
28. Grosdidier T, Hazotte A, Simon A (1998) Precipitation and dissolution processes in γ/γ′ single crystal nickel-based superalloys. Mat Sci Eng A 256:183–196. https://doi.org/10.1016/S0921-5093(98)00795-3
29. Adil Ali M, Shchyglo O, Stricker M, Steinbach I (2023) Coherency loss marking the onset of degradation in high temperature creep of superalloys: phase-field simulation coupled to strain gradient crystal plasticity. Comp Mat Sci 220:112069. https://doi.org/10.1016/j.commatsci.2023.112069
30. Li L, Gong X, Wang C, Wu Y, Yu H, Su H, Zhou L (2021) Correlation between phase stability and tensile properties of the Ni-based superalloy MAR-M247. Acta Metall Sin (Eng Lett) 34:872–884. https://doi.org/10.1007/s40195-020-01139-4
31. Buyakova SP, Dedova ES, Wang D, Mirovoy Y, Burlachenko AG, Buyakov AS (2022) Phase evolution during entropic stabilization of ZrC, NbC, HfC, and TiC. Ceram Inter 48(8):11747–11755. https://doi.org/10.1016/j.ceramint.2022.01.033
32. Murata Y, Suga K, Yukawa N (1986) Effect of transition elements on the properties of MC carbides in IN-100 nickel-based superalloy. J Mater Sci 21(10):3653–3660. https://doi.org/10.1007/BF00553814
33. Donachie MJ, Donachie SJ (2002) Superalloys: a technical guide. ASM International, Materials Park, OH, USA
34. Liu L, Zhen BL, Banerji A, Reif W, Sommer F (1994) Effect of melt homogenization temperature on the cast structures of IN738LC superalloy. Scr Metall et Mater 30(5):593–598. https://doi.org/10.1016/0956-716X(94)90435-9
35. Chen TC, Cheng YH, Tsay LW, Shiue RK (2018) Effects of grain boundary microconstituents on heat-affected zone cracks in a Mar-M004 Weldment. Met 8:201. https://doi.org/10.3390/met8040201
36. Liu G, Kong L, Ruan S, Birosca S (2021) Microstructure and phases structure in nickel-based superalloy IN713C after solidification. Mat Charact 182:111566. https://doi.org/10.1016/j.matchar.2021.111566
37. Wang C, Guo Y, Guo J, Zhou L (2015) Microstructural stability and mechanical properties of a boron modified Ni–Fe based superalloy for steam boiler applications. Mat Sci Eng A 639:380–388. https://doi.org/10.1016/j.msea.2015.05.026
38. Xiao L, Chen DL, Chaturvedi MC (2006) Effect of boron on fatigue crack growth behavior in superalloy IN 718 at RT and 650°C. Mater Sci Eng A 428(1-2):1–11. https://doi.org/10.1016/j.msea.2005.08.206
39. Tytko D, Choi PP, Klöwer J, Kostka A, Inden G, Raabe D (2012) Microstructural evolution of a Ni-based superalloy (617B) at 700 °C studied by electron microscopy and atom probe tomography. Acta Mater 60(4):1731–1740. https://doi.org/10.1016/j.actamat.2011.11.020
40. Huang HE, Koo CH (2004) Characteristics and mechanical properties of polycrystalline CM 247 LC superalloy casting. Mat Trans 45(2):562–568. https://doi.org/10.2320/matertrans.45.562
41. Rame J, Eyidi D, Joulain A, Gauthe M, Cormier J (2023) Creep and tensile behavior of a nickel-based single crystal superalloy with a bimodal γ′ precipitation. Metall Mater Trans A 54:1496–1508. https://doi.org/10.1007/s11661-023-07022-y
42. Hamadi S, Hamon F, Delautre J, Cormier J, Villechaise P, Utada S, Kontis P, Bozzolo N (2018) Consequences of a room-temperature plastic deformation during processing on creep durability of a Ni-based SX superalloy. Metall Mater Trans A 49:4246–4261. https://doi.org/10.1007/s11661-018-4748-3
43. le Graderend JB, Cormier J, Gallerneau F, Villechaise P, Kruch S, Mendez J (2014) A microstructure-sensitive constitutive modeling of the inelastic behavior of single crystal nickel-based superalloys at very high temperature. Int J Plast 59:55–83. https://doi.org/10.1016/j.ijplas.2014.03.004
44. Westbrook J (1957) Temperature dependence of the hardness of secondary phases common in turbine bucket alloys. J Min Met Mater Soc 9:898–904. https://doi.org/10.1007/BF03397938
45. Beardmore P, Davies R, Johnston T (1969) On the temperature dependence of the flow stress of nickel-base alloys. Trans Metall Soc AIME 245:1532–1545